# Wettability in complex porous materials, the mixed-wet state, and its relationship to surface roughness

Ahmed AlRatrout[a,1], Martin J. Blunt[a], and Branko Bijeljic[a]

[a]Department of Earth Science and Engineering, Imperial College London, London SW7 2AZ, United Kingdom

Edited by David A. Weitz, Harvard University, Cambridge, MA, and approved July 17, 2018 (received for review March 3, 2018)

**A quantitative in situ characterization of the impact of surface roughness on wettability in porous media is currently lacking. We use reservoir condition micrometer-resolution X-ray tomography combined with automated methods for the measurement of contact angle, interfacial curvature, and surface roughness to examine fluid/fluid and fluid/solid interfaces inside a porous material. We study oil and water in the pore space of limestone from a giant producing oilfield, acquiring millions of measurements of curvature and contact angle on three millimeter-sized samples. We identify a distinct wetting state with a broad distribution of contact angle at the submillimeter scale with a mix of water-wet and water-repellent regions. Importantly, this state allows both fluid phases to flow simultaneously over a wide range of saturation. We establish that, in media that are largely water wet, the interfacial curvature does not depend on solid surface roughness, quantified as the local deviation from a plane. However, where there has been a significant wettability alteration, rougher surfaces are associated with lower contact angles and higher interfacial curvature. The variation of both contact angle and interfacial curvature increases with the local degree of roughness. We hypothesize that this mixed wettability may also be seen in biological systems to facilitate the simultaneous flow of water and gases; furthermore, wettability-altering agents could be used in both geological systems and material science to design a mixed-wetting state with optimal process performance.**

roughness | complex porous media | in situ reservoir conditions | contact angle | curvature

Determining how carbon dioxide can be stored securely in underground aquifers, quantifying the rate at which oil and gas are recovered from hydrocarbon reservoirs and shale, the performance of fuel cells and catalysts, the efficiency of gas exchange in leaves and lungs, how well fabrics resist or soak up water, and the design of water-repellent surfaces all crucially depend on wettability: how fluid phases interact with solid surfaces within porous structures. From a fundamental point of view, it is still unknown how wettability controls the fluid configurations in porous materials and what drives the formation of fluid layers leading to either enhanced or impeded flow and transport (1–6).

The interaction of fluids with a rough surface is traditionally described using the model of Wenzel (7) or the theory of Cassie and Baxter (8), which are used to calculate a single effective contact angle on a rough surface (9, 10). This approach has been used to interpret the transition from water-wet (WW) to water-repelling conditions in human skin, leaves, insect wings, feathers, and manufactured surfaces for instance (2, 3, 11, 12). However, this work deals with external surfaces and does not quantify the typical wetting states within a material and the relationship with surface roughness: for example, what are the contact angles and fluid arrangements inside a leaf, lung tissue, or rocks, and how do they affect fluid flow?

In porous rocks, where portions of the solid surface have undergone a wettability alteration caused by the direct contact of surface-active components with the solid (13), it has been suggested that separated WW and oil-wet (OW) regions of the pore space are present (14, 15), and this has been observed directly using atomic force microscopy in chalk (16). The advent of high-resolution X-ray microtomography has made it possible to image the rock and fluids within the pore space at micrometer resolution (for instance, refs. 17 and 18) and from this, to determine contact angles directly at the high temperatures and pressures representative of deep underground reservoirs (18–21). The behavior is somewhat different from the theory: a wide distribution of contact angle is seen, even in mineralogically homogeneous rocks (22). Contact angle values both above and below 90° are observed, with local variations over a pore scale of around 100 μm (23), allowing both oil and water to remain connected in wetting layers that can flow over a wide range of saturation, which is favorable for oil recovery (15, 22) (Fig. 1). Fluid/fluid interfacial curvature from which a local capillary pressure can be derived has also been measured, but the values have not been related to surface roughness and pore size (24, 25). The range of observed contact angles is likely to be a result of the roughness of the rock surfaces. However, methods to quantify roughness have been concerned with the external surfaces of objects and are not directly applicable to porous materials (26–29). We quantify surface roughness and find its relationship with

## Significance

**In many important processes that control $CO_2$ storage in aquifers, oil recovery, and gas exchange in leaves, for instance, flow is controlled by the interaction of immiscible fluids with a rough surface. We use micrometer-resolution X-ray imaging to look inside millimeter-sized porous structures, obtaining millions of measurements of contact angle and interfacial curvature. We quantify the relationship between surface roughness and wettability. Rougher surfaces are associated with lower contact angles and higher interfacial curvatures. We identify a distinct mixed-wet state where two fluid phases remain connected over a wide range of saturation. This state can be designed to improve oil recovery or the performance of fuel cells, catalysts, and other porous materials.**

Author contributions: A.A., M.J.B., and B.B. designed research; A.A. performed research; A.A., M.J.B., and B.B. contributed new analytic tools; A.A., M.J.B., and B.B. analyzed data; and A.A., M.J.B., and B.B. wrote the paper.

The authors declare no conflict of interest.

This article is a PNAS Direct Submission.



Data deposition: The data reported in this paper are available at www.digitalrocksportal.org/projects/151 and www.github.com/AhmedAlratrout/ContactAngle-Curvature-Roughness.

[1]To whom correspondence should be addressed. Email: a.alratrout14@imperial.ac.uk.

This article contains supporting information online at www.pnas.org/lookup/suppl/doi:10.1073/pnas.1803734115/-/DCSupplemental.

Published online August 17, 2018.

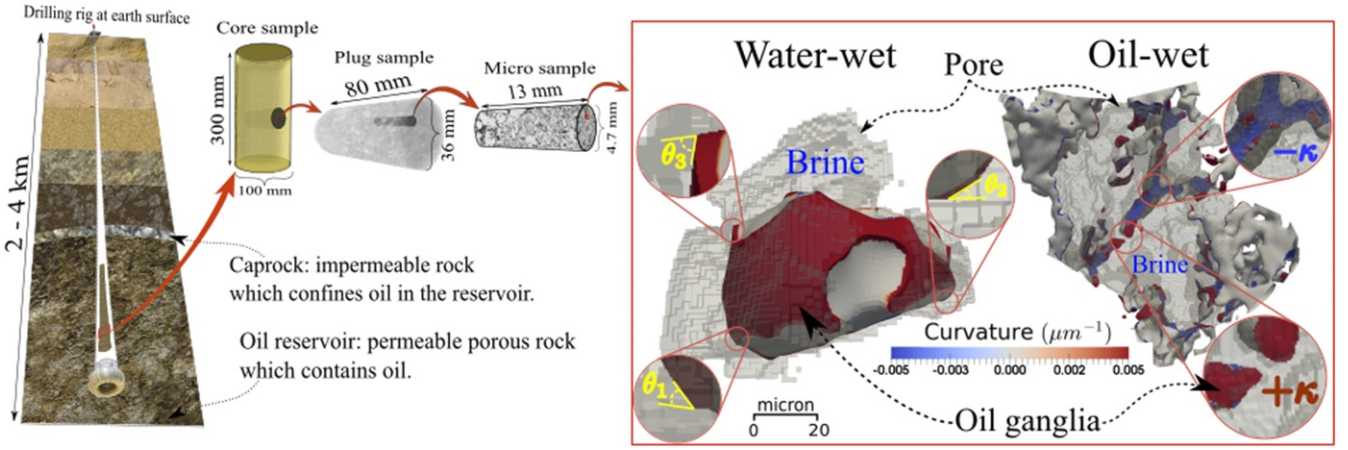


**Fig. 1.** A schematic of wettability and length scales in porous media flows. *Right* shows images of oil retained within the pore space of WW and OW samples. The curvature of the oil/brine interface is indicated by the colors, while the solid surface in contact with brine is shown in gray. In a WW rock, the oil is trapped in quasispherical ganglia with contact angles less than 90°. For an OW rock, oil is retained in layers that follow the surface roughness with both positive and negative values of the curvature $\kappa$. This allows the oil to flow to low saturation, facilitating recovery at the kilometer scale (*Left*). *Center* shows how the samples are selected from centimeter-scale cores extracted from a reservoir.

local values of contact angle and fluid/fluid curvature measured on pore space images (30). We then discuss the implications that our findings have for oil recovery, carbon dioxide storage, and other processes.

## Distributions of Contact Angle, Curvature, and Roughness

We image oil and brine in the pore space of three rock samples after water flooding. The methods for obtaining contact angle, curvature, and surface roughness are shown in Fig. 2 (*Materials and Methods* has more details) and applied to find a total of 54.2 million in situ measurements. In what follows, we will look for relationships between these quantities on a point-by-point basis and between their pore averages. We will find a relationship between surface roughness, contact angle, and interfacial curvature as well as between the variation in contact angle and interfacial curvature within a pore and the average roughness.

In the experiments, we waited for 2 h after the end of water flooding before imaging the fluid distribution. We assume that the contact angles and interfacial curvature are constant and represent equilibrium conditions. However, it is possible that the fluids are still moving, albeit slowly (5, 31–33). In any event, in what follows, we show how the interfacial curvature and contact angle are related to surface roughness.

Fig. 3 *A* and *B* shows the wide range of the measured distributions of contact angle and interfacial curvature for the three samples studied. The average contact angles are 76°, 93°, and 103°: the differences are caused by exposing the samples to different crude oils at different temperatures (22) (*SI Appendix*). We will label the three samples WW, mixed-wet (MW), and OW in what follows. On flat calcite surfaces, using the same fluids, the measured contact angles were 76°, 130°, and 141°. For the MW and OW samples, the in situ angles were, on average, lower than those measured on a flat surface, indicating that surface roughness tends to reduce the apparent oil wetness of the rock. The distributions of both contact angle and interfacial curvature are widest for the MW and OW samples and sharpest for the WW case.

The accuracy of the contact angle and curvature measurements was tested in refs. 30 and 23, respectively, using synthetic images with different resolutions of known curvature and contact angle. We are able to estimate contact angle to within 3° and curvature with an error less than 9% when the sphere is two or more voxels across, which indicates that, with a 2-μm voxel size, we can accurately capture curvatures as high as 0.5 $\mu m^{-1}$ and contact angles on pores 4 μm across.

The oil saturation values after 20 pore volumes of water injection in the entire volume of the samples (Fig. 2*A*) are 0.329, 0.159, and 0.412 for the WW, MW, and OW samples,

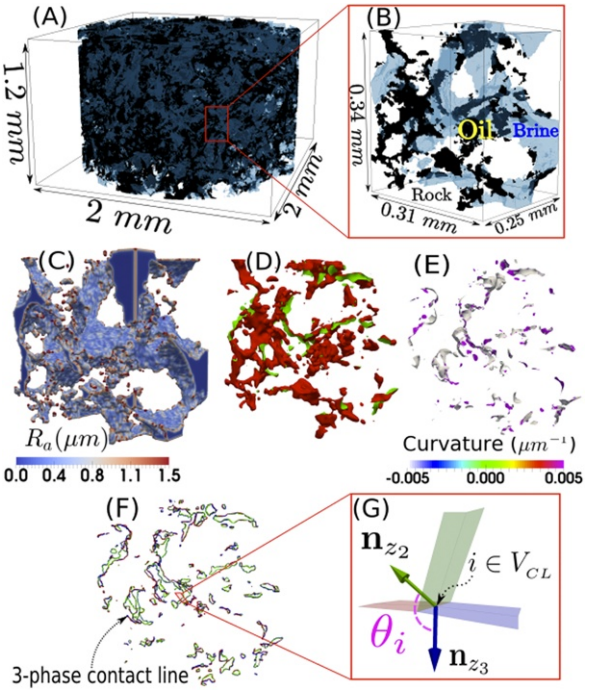


**Fig. 2.** Roughness, contact angle, and oil/brine interface curvature measurements. (*A*) A 3D view of the raw segmented dataset of the OW sample with a voxel size of 2 μm. (*B*) The oil (black) and brine (blue) phases are shown in a zoomed-in section of the image. (*C*) The curvature-based roughness measurement ($R_a$) on each vertex belonging to the rock surface after applying uniform-curvature smoothing: the smooth and rough areas are indicated by blue and red, respectively. (*D*) The smoothed mesh that is found after applying both Gaussian and curvature smoothing: the identified interfaces oil/brine (green) and oil/solid (red). (*E*) The measured curvature values of all vertices belonging to the oil/brine interface. (*F*) The extracted three-phase contact line. (*G*) Normal vectors are defined on both the oil/brine and the brine/rock interfaces at the three-phase contact line: the cosine of the contact angle is calculated from the dot product of these two normals.

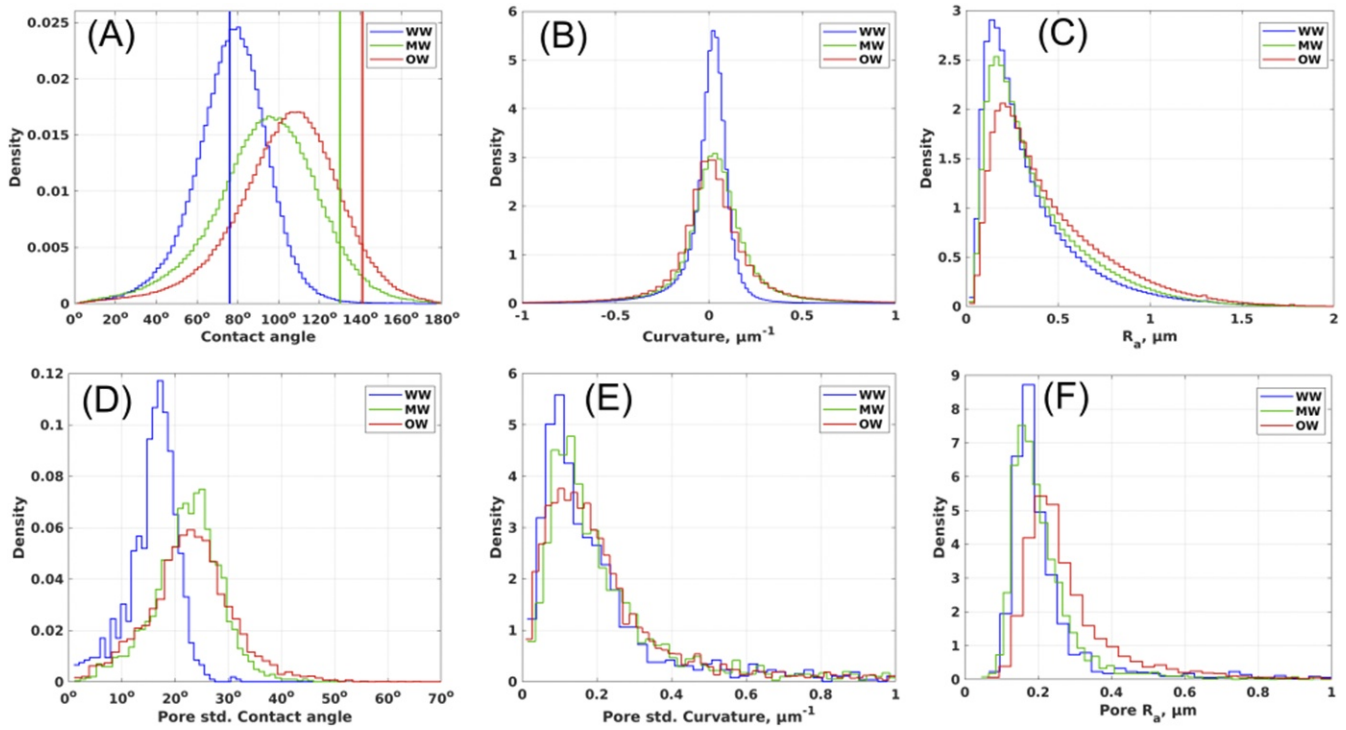


**Fig. 3.** Distributions of the measurements on pore space images. *A–C* show point-by-point values, while *D–F* show pore-averaged values. (*A*) Histogram of all of the contact angle measurements, where the values measured on a flat surface are indicated by the vertical lines. (*B*) Histogram of the measured oil/brine interfacial curvature. (*C*) The distribution of surface roughness. (*D*) The variation of contact angle and (*E*) oil/brine interface curvature using the SD per pore. In addition, the pore-averaged (mode) curvature-based roughness, $R_a$ (*F*) in each pore is shown for the three samples: WW (blue), MW (green), and OW (red). Std. indicates SD.

respectively: the MW condition with contact angles broadly distributed above and below 90° gives the most favorable recovery. This is a direct consequence of the mixed-wettability state that enhances oil connectivity and allows flow of both oil and water over a wide range of saturation.

In Fig. 3*C*, we plot the distribution of roughness quantified by the area-weighted absolute value of the solid surface curvature (Eq. **1**) (*Materials and Methods*), with magnitude that indicates the deviation of the surface from a plane measured at the scale of a single voxel 2 μm across. The roughness is measured in pores where oil is present: we see slightly higher roughness values for the OW case, since the oil resides in small pores with high surface curvatures (*SI Appendix*, Fig. S3 *A–C*).

In Fig. 3 *D* and *E*, we show the variation of contact angle and interfacial curvature using the calculated standard deviation (SD) in each pore. Also, in Fig. 3*F*, we show the pore-averaged mode value of roughness to represent a typical value in a pore. Pores are defined using a generalized network extraction algorithm (34) (*Materials and Methods*). Within each pore, we observe a wide distribution of contact angle and interfacial curvature. The exception is the WW case, which has a relatively narrow SD of contact angle (Fig. 3*D*) and to a lesser extent, curvature (Fig. 3*E*). In a WW rock, the oil resides in quasispherical trapped ganglia (Fig. 1) that have an approximately constant curvature. In contrast, in the MW and OW samples, a pore may contain several separate layers that tend to follow the surface roughness, and we observe larger values of the SD and of curvature and contact angle. The surface roughness varies from pore to pore (Fig. 3*F*). Now, we will study the relationship between roughness, curvature, and contact angle.

## Correlation of Contact Angles, Curvatures, and Roughness

Fig. 4 shows the point-by-point correlation between surface roughness and both contact angle and interfacial curvature as a function of the distance between the measurements (Eq. **5**). With a complex pore geometry and fluid arrangement in a natural system, we do not expect to have an exact relationship between the variables; nevertheless, the following trends are clear. Fig. 4 *A–C* shows that the local surface roughness varies spatially with a correlation length that is around a pore size: we see variations of roughness both within and between pores (Fig. 3*F*). This correlation is also seen for contact angle and interfacial curvature (*SI Appendix*, Fig. S2).

For the MW and OW cases, the roughness is anticorrelated with contact angle (Fig. 4 *E* and *F*), meaning that rougher surfaces are associated with lower values of the contact angle. This explains two hitherto unobserved features of wettability, namely that the average contact angle is lower than that measured on a flat calcite surface at the same conditions and with the same fluids and why there is a wide range of contact angle. Water collects in grooves, invaginations, and other high-curvature portions of the surface (Fig. 1). The effective angle for a displacement is a combination of advance over this water in corners (with a zero angle) and over altered wettability surfaces where oil has contacted the solid directly. The result is—on average—lower contact angles, albeit with a large variation—with a greater shift toward more WW conditions associated with rougher surfaces that are able to retain more water after primary drainage. For the WW sample (Fig. 4*D*), the correlation is weaker, since the wettability alteration is less significant. For interfacial curvature (Fig. 4 *G–I*), we see a positive correlation in that more roughness, associated with slightly more WW conditions, is associated with larger curvatures.

In Fig. 5, we study on a pore-by-pore basis the correlation ($\rho$) between the SD of contact angle, oil/brine interfacial curvature, and roughness as a function of pore diameter: each point is calculated for a pore diameter interval of 10 μm (Eq. **6**).

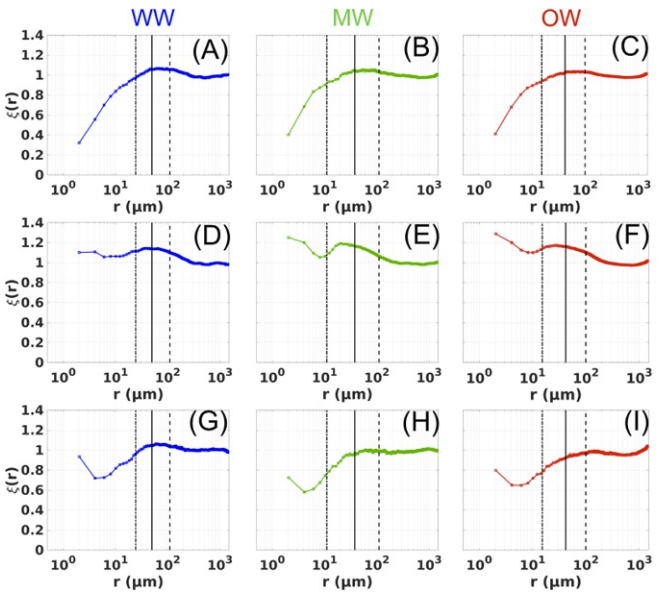


**Fig. 4.** Spatial correlations computed using Eq. **5**. (*A–C*) The spatial correlation of surface roughness ($R_a$). We see a correlation length of approximately a pore size. (*D–F*) The correlation between surface roughness and contact angle as a function of the distance between the measurements. Here, a value of $\xi > 1$ indicates an anticorrelation in that greater roughness is associated with smaller contact angles. (*G–I*) The correlation between surface roughness and interfacial curvature. Here, rougher surfaces, which tend to be more WW, are more likely to have a higher interfacial curvature ($\xi < 1$) for the MW and OW samples, consistent with the results in *D–F*. The vertical lines indicate the minimum pore diameter (dotted), the average pore diameter (solid), and the maximum pore diameter (dashed).

$\rho = 1$ indicates a strong correlation, while 0 is no correlation. We see a correlation between the variation of contact angle and roughness (Fig. 5 *A–C*) that is more evident in the larger pores, where more measurements can be taken (Fig. 5 *D–F*) and for which the roughness is unrelated to pore size (*SI Appendix*, Fig. S3 *A–C*). On a rough surface, the effective angle, measured at the resolution of the image, may differ significantly from the intrinsic local angle at the molecular scale. We suggest that, for rougher surfaces, we see a greater range of contact angle, since there are more deviations from the average than would be seen on a smooth surface; in addition, this variation is caused by the retention of water in crevices in the pore space, with lower average contact angles seen for rougher surfaces (Fig. 4 *D–F*). The WW sample shows little or no correlation between curvature and roughness (Fig. 5*G*). The reason for this is that the oil tends to reside as quasispherical droplets in the larger pores (Fig. 1) as previously discussed, with an overall positive oil/brine interface curvature indicative of the capillary pressure at which the oil ganglion was trapped. For the MW and OW samples, oil layers form that coat portions of the solid surface; a rough surface experiences a wide variation in local curvature, and hence, we see a relationship between the variation of oil/brine interface curvature and surface roughness (Fig. 5 *H* and *I*). This effect is again more evident in the larger pores, where a more representative fraction of the surface is covered with oil (Fig. 5 *K* and *L*). Note that it is wrong to associate an OW rock surface with a negative oil/brine interfacial curvature in a pore: consider an OW drop on a surface surrounded by water—the drop has a positive curvature even when the contact angle is greater than 90°.

## Conclusions and Outlook

In WW media with little wettability alteration on contact with crude oil, the interfacial curvature is approximately constant and positive. The nonwetting phase (oil in this case) is trapped as quasispherical ganglia in the larger pore spaces. This is optimal for storage applications, such as carbon dioxide sequestration, where it is desirable to trap one phase in the pore space to prevent migration and escape. However, this is not ideal for oil recovery or other processes, such as gas transport through membranes or in biological tissues for instance, where it is necessary to allow the flow of both fluids.

In rocks with an altered wettability, we observe oil layers that tend to follow the local curvature of the surface. The range of the distribution of contact angle and curvature increases with the degree of roughness, with the correlation more obvious in larger pores and for a stronger wettability change. The contact angle tends to be lower on rougher surfaces due to the accumulation of water in crevices, which makes the surface effectively less oil wetting. We have an MW state with a wide range of local contact angles both above and below 90°. This facilitates the flow of both phases, which is favorable for oil recovery (22). It is well-understood that, using surfactants or changing the brine salinity, oil recovery can be improved through changing the wettability (35, 36). However, we suggest that an MW state is ideal, which contrasts with the current assumption that moving toward a more uniformly WW state is preferred (37).

We hypothesize that, in other porous materials, where it is desirable to allow both a liquid phase and a gas phase to flow over a wide range of saturation, the combination of wettability alteration and rough surfaces leads to an MW state, where roughness drives a naturally water-repellent surface to have a range of

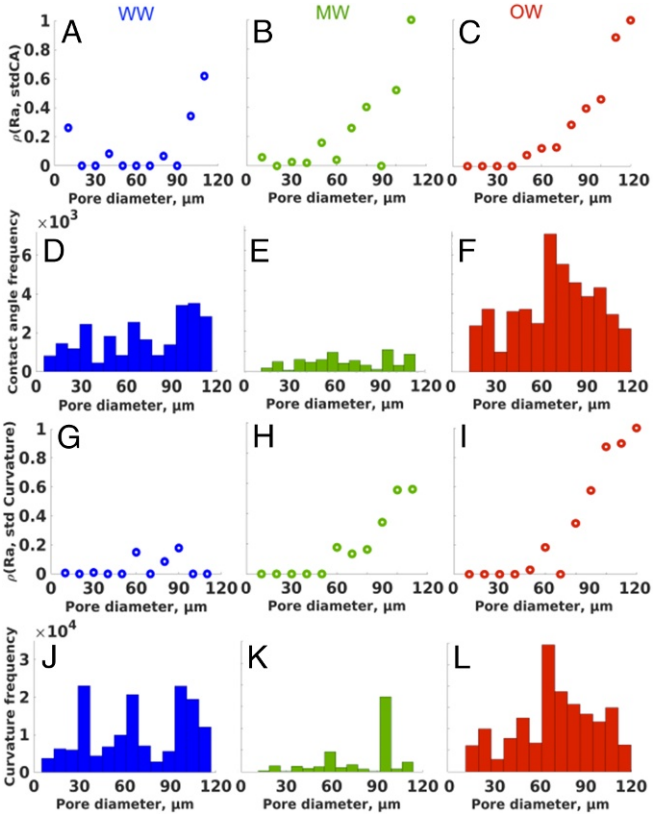


**Fig. 5.** Relationship between the variation in contact angle, interfacial curvature, and surface roughness using Eq. **6**. The calculated correlation ($\rho$) of pore-averaged curvature-based roughness ($R_a$) with measured contact angle (*A–C*) and oil/brine interface curvature variation (*G–I*) is shown as a function of pore diameter. Where $\rho = 1$, the two variables are strongly correlated. Also shown in *D–F* and *J–L* is the number of data points considered for each pore size: most of the data comes from the larger pores. Std. indicates SD.

effective contact angle. This could be tested, for instance, in leaves, lung tissue, and multiphase catalysts using the image and analysis methodology proposed here. Furthermore, such a wettability state could be designed to improve the performance of fuel cells (38), catalysts, membranes, and other porous materials.

## Materials and Methods

**Experiments.** The experiments were conducted on three rock samples of 4.8 mm in diameter and a length between 13 and 16 mm from a giant multibillion barrel carbonate oil reservoir in the Middle East, which is mainly composed of calcite ($96.5 \pm 1.9$ wt %). The experimental procedure follows the same protocols described in ref. 22, to which the reader is referred for additional details. The experimental workflow is as follows.

*i*) $CO_2$ was injected into the clean and dry samples to displace air followed by brine injection to fully saturate the rock.
*ii*) Subsurface conditions were established (60°C or 80°C and 10 MPa), and primary drainage (crude oil injection) was performed followed by aging over 3 weeks to restore rock wettability.
*iii*) During brine injection, the flow was reversed, and 20 pore volumes of brine was injected at a low flow rate of 15 μL/min, corresponding to a capillary number of $6 \times 10^{-7}$ for the WW and OW samples and $3 \times 10^{-7}$ for the MW sample. Fluids were allowed to reach equilibrium for 2 h before acquiring high-resolution (2 μm per voxel) scans.

All images were acquired using the Xradia VersaXRM-500 X-ray microscope; the images were segmented into three phases (oil, brine, rock) from the raw micro-CT image using a machine learning-based image segmentation known as Trainable WEKA Segmentation (39). The size of the segmented images in voxels is $435 \times 10^6$ for all samples for a part of the rock samples with a diameter of 1.9 mm and a length of 1.2 mm (volume of approximately 3.4 $mm^3$). We calculated oil saturation values directly from the image by summing the number of voxels belonging to the oil phase and dividing by the void space, which is represented by the total number of voxels containing both brine and oil phases.

**Rock Surface Roughness.** We generate a mesh to represent the rock surface; for this, we define the vertex area for each point *i* identified on the surface ($A_i$). Then, we apply a volume-preserving curvature smoothing, which removes the voxelized artifacts from the segmented image: we measure the curvature, $\kappa$, for each vertex (30) (Fig. 2).

We estimate the surface roughness for each vertex ($R_{a_i}$) as

$$R_{ai} = \frac{1}{N} \sum_{j \in adj(i)}^{N} |\kappa_j \mathbf{A}_j|, \quad [1]$$

where $\kappa_j$ and $\mathbf{A}_j$ are the computed curvature and area of the nearest neighbor vertices (*j*) on the rock surface, respectively, and *N* is the number of nearest neighbor vertices. Note that we use the modulus of the curvature, so that $R_a$ is always positive and has units of length. Surface roughness was only measured in pores that contained oil.

**Contact Angle and Fluid/Fluid Interfacial Curvature.** The calculation of contact angle and interfacial curvature is described in ref. 30, to which the reader is referred for additional details (Fig. 2).

**Associating Roughness, Fluid/Fluid Curvature, and Contact Angle Measurements on a Pore-by-Pore Basis.** A generalized pore network model (34) generated a partitioning of the void space, allowing the measurements to be linked to specific pores. A pore center is a local maximum in the distance map—the distance from any point in the void space to the nearest solid surface. The region of the void space where the distance map increases toward a particular pore center is assigned to that pore. Similarly, all roughness, curvature, and contact angle values can be assigned a pore label. The WW, MW, and OW samples had 4,719, 5,643, and 8,858 pores, respectively, of which 1,092, 2,930, and 5,322 contained three-phase contact points.

**Correlation Functions.** We consider two variables *x* and *y* that are measured at discrete points *i* and *j*: *x* is the solid surface roughness defined as $x_i = R_{ai}$ (Eq. **1**), while *y* is the contact angle, the fluid/fluid interfacial curvature, or the roughness itself.

We define dimensionless variables $\tilde{x}_i$ and $\tilde{y}_i$:

$$\tilde{x}_i = \frac{x_i - \bar{x}}{\sigma_x}, \quad [2]$$

where $\bar{x}$ is the average value of *x* measured over the entire distribution

$$\bar{x} = \frac{1}{N_x} \sum_{i=1}^{N_x} x_i, \quad [3]$$

and $N_x$ is the total number of values of *x*. $\tilde{y}_i$ is defined in a similar manner. $\sigma_x$ is the SD

$$\sigma_x^2 = \frac{1}{N_x} \sum_{i=1}^{N_x} (x_i - \bar{x})^2. \quad [4]$$

Then, we define a correlation $\xi(r)$ as

$$\xi(r) = \frac{\sum_{j=1}^{N_y} \sum_{i=1}^{N_x} I_{ij} (\tilde{x}_i - \tilde{y}_j)^2}{2 \sum_{j=1}^{N_y} \sum_{i=1}^{N_x} I_{ij}}, \quad [5]$$

where $I_{ij}$ is an indicator function: if $r_{ij}$ is the distance between the locations *i* and *j* where *x* and *y* are measured, then $I_{ij} = 1$ if $r + \epsilon > r_{ij} > r - \epsilon$ and 0 otherwise, where $\epsilon = 1$ μm here.

A value $\xi = 1$ represents no correlation and is expected for $r \to \infty$ and for variables that have no relationship with each other. $\xi = 0$ is a perfect correlation and would be seen at $r = 0$ if *x* and *y* were the same variable; $\xi > 1$ represents an anticorrelation. The value at $r = 0$ where *x* and *y* represent different quantities is a measure of how well they are related at the same location.

We also define the correlations between pore-averaged values:

$$\rho(d) = \frac{\sum_{i=1}^{N_p} I_i \tilde{x}_i \tilde{y}_i}{\sum_{i=1}^{N_p} I_i}, \quad [6]$$

where now the indicator function labels a pore with a diameter of a particular bin size, *d*. The sums are over the number of pores $N_p$, while $\tilde{x}_i$ and $\tilde{y}_i$ represent pore-averaged values of the variation in contact angle or curvature and surface roughness, respectively. Here, $\rho = 0$ indicates no correlation, while $\rho = 1$ represents perfectly correlated variables.

**ACKNOWLEDGMENTS.** We thank Amer Alhammadi for sharing his experimental dataset. Also, we thank Ali Raeini for sharing his codes to extract the segmented pore images. We acknowledge Abu Dhabi National Oil Company for financial support and permission to publish the data.

1. de Gennes PG (1985) Wetting: Statics and dynamics. *Rev Mod Phys* 57:827–863.
2. Sanchez C, Arribart H, Madeleine M, Guille G (2005) Biomimetism and bioinspiration as tools for the design of innovative materials and systems. *Nat Mater* 4:277–288.
3. Sun T, Feng L, Gao X, Jiang L (2005) Bioinspired surfaces with special wettability. *Acc Chem Res* 38:644–652.
4. Datta SS, Dupin JB, Weitz DA (2014) Fluid breakup during simultaneous two-phase flow through a three-dimensional porous medium. *Phys Fluids* 26:062004.
5. Zhao B, MacMinn CW, Juanes R (2016) Wettability control on multiphase flow in patterned microfluidics. *Proc Natl Acad Sci USA* 113:10251–10256.
6. Reynolds CA, Menke H, Andrew M, Blunt MJ, Krevor S (2017) Dynamic fluid connectivity during steady-state multiphase flow in a sandstone. *Proc Natl Acad Sci USA* 114:8187–8192.
7. Wenzel RN (1936) Resistance of solid surfaces to wetting by water. *Ind Eng Chem* 28:988–994.
8. Cassie ABD, Baxter S (1944) Wettability of porous surfaces. *Trans Faraday Soc* 40:546–551.
9. Hirasaki GJ (1991) Wettability: Fundamentals and surface forces. *SPE Formation Eval* 6:217–226.
10. Lafuma A, Quéré D (2003) Superhydrophobic states. *Nat Mater* 2:457–460.
11. Nychka JA, Gentleman MM (2010) Implications of wettability in biological materials science. *JOM* 62:39–48.
12. Bromberg L et al. (2017) Control of human skin wettability using the ph of anionic surfactant solution treatments. *Colloids Surf B Biointerfaces* 157:366–372.
13. Buckley JS, Takamura K, Morrow N (1989) Influence of electric surface charges on the wetting properties of crude oils. *SPE Res Eng* 4:332–340.
14. Kovscek A, Wong H, Radke C (1993) A pore-level scenario for the development of mixed wettability in oil reservoirs. *Environ Energy Eng* 39:1072–1085.
15. Blunt MJ (2017) *Multiphase Flow in Permeable Media: A Pore-Scale Perspective* (Cambridge Univ Press, Cambridge, MA), p 500.

16. Hassenkam T, Skovbjerg L, Stipp S (2009) Probing the intrinsically oil-wet surfaces of pores in north sea chalk at subpore resolution. *Proc Natl Acad Sci USA* 106:6071–6076.
17. Berg S et al. (2013) Real-time 3d imaging of haines jumps in porous media flow. *Proc Natl Acad Sci USA* 110:3755–3759.
18. Pak T, Butler I, Geiger S, van Dijke M, Sorbie K (2015) Droplet fragmentation: 3D imaging of a previously unidentified pore-scale process during multiphase flow in porous media. *Proc Natl Acad Sci USA* 112:1947–1952.
19. Andrew M, Bijeljic B, Blunt MJ (2014) Pore-scale contact angle measurements at reservoir conditions using x-ray microtomography. *Adv Water Resour* 68:24–31.
20. Khishvand M, Alizadeh AH, Piri M (2016) In-situ characterization of wettability and pore-scale displacements during two- and three-phase flow in natural porous media. *Adv Water Resour* 97:279–298.
21. Khishvand M, Alizadeh AH, Kohshour IO, Piri M, Prasad RS (2017) In situ characterization of wettability alteration and displacement mechanisms governing recovery enhancement due to low-salinity waterflooding. *Water Resour Res* 53:4427–4443.
22. Alhammadi AM, AlRatrout A, Singh K, Bijeljic B, Blunt MJ (2017) In situ characterization of mixed-wettability in a reservoir rock at subsurface conditions. *Sci Rep* 7:10753.
23. AlRatrout AAM, Blunt MJ, Bijeljic B (July 2, 2018) Spatial correlation of contact angle and curvature in pore-space images. *Water Resour Res*, in press.
24. Armstrong RT, Porter ML, Wildenschild D (2012) Linking pore-scale interfacial curvature to column-scale capillary pressure. *Adv Water Resour* 46:55–62.
25. Andrew M, Bijeljic B, Blunt MJ (2014) Pore-by-pore capillary pressure measurements using X-ray microtomography at reservoir conditions: Curvature, snap-off, and remobilization of residual $CO_2$. *Water Resour Res* 50:8760–8774.
26. Xie H, Wang J, Kwaśniewski MA (1999) Multifractal characterization of rock fracture surfaces. *Int J Rock Mech Mining Sci* 36:19–27.
27. Leach RK, et al. (2008) *Guide to the Measurement of Smooth Surface Topography Using Coherence Scanning Interferometry* (Queen's Printer for Scotland, Middlesex, UK).
28. Mah J, Samson C, McKinnon SD (2011) 3D laser imaging for joint orientation analysis. *Int J Rock Mech Mining Sci* 48:932–941.
29. Lai P, Samson C, Bose P (2014) Surface roughness of rock faces through the curvature of triangulated meshes. *Comput Geosciences* 70:229–237.
30. AlRatrout A, Raeini AQ, Bijeljic B, Blunt MJ (2017) Automatic measurement of contact angle in pore-space images. *Adv Water Resour* 109:158–169.
31. Armstrong RT, Berg S (2013) Interfacial velocities and capillary pressure gradients during haines jumps. *Phys Rev E* 88:043010.
32. Edery Y, Berg S, Weitz D (2018) Surfactant variations in porous media localize capillary instabilities during haines jumps. *Phys Rev Lett* 120:028005.
33. Alizadeh Pahlavan A, Cueto-Felgueroso L, Hosoi AE, McKinley GH, Juanes R (2018) Thin films in partial wetting: Stability, dewetting and coarsening. *J Fluid Mech* 845:642–681.
34. Raeini AQ, Bijeljic B, Blunt MJ (2017) Generalized network modeling: Network extraction as a coarse-scale discretization of the void space of porous media. *Phys Rev E* 96:013312.
35. Morrow NR (1990) Wettability and its effect on oil recovery. *J Pet Technol* 42:1476–1484.
36. Jerauld G, Rathmell J (1997) Wettability and relative permeability of Prudhoe Bay: A case study in mixed-wet reservoirs. *SPE Reservoir Eng* 12:58–65.
37. Morrow N, Buckley J (2011) Improved oil recovery by low-salinity waterflooding. *J Pet Technol* 63:106–112.
38. Grey C, Tarascon J (2017) Sustainability and *in situ* monitoring in battery development. *Nat Mater* 16:45–56.
39. Arganda-Carreras I, et al. (2017) Trainable weka segmentation: A machine learning tool for microscopy pixel classification. *Bioinformatics* 33:2424–2426.